Phase Engineering of MXene Derivatives Via Molecular Design for High-Rate Sodium-Ion Batteries

Hui Zhang, Xingwu Zhai, Xin Cao, Zhihao Liu, Xinfeng Tang, Zhihong Hu, Hang Wang, Zhandong Wang, Yang Xu (iD)*, Wei He, Wei Zheng** (iD)*, Min Zhou**, and ZhengMing Sun**

Since 2019, research into MXene derivatives has seen a dramatic rise; further progress requires a rational design for specific functionality. Herein, through a molecular design by selecting suitable functional groups in the MXene coating, we have implemented the dual N doping of the derivatives, nitrogen-doped TiO_2@nitrogen-doped carbon nanosheets (N-TiO_2@NC), to strike a balance between the active anatase TiO_2 at low temperatures, and carbon activation at high temperatures. The NH_3 reduction environment generated at 400 °C as evidenced by the in situ pyrolysis SVUV-PIMS process is crucial for concurrent phase engineering. With both electrical conductivity and surface Na^+ availability, the N-TiO_2@NC achieves higher interface capacitive-like sodium storage with long-term stability. More than 100 mAh g^{-1} is achieved at 2 A g^{-1} after 5000 cycles. The proposed design may be extended to other MXenes and solidify the growing family of MXene derivatives for energy storage.

1. Introduction

Sodium-ion batteries (SIBs) represent a potential supplementary to lithium-ion batteries.[1–4] Because of the sluggish kinetics of large radius sodium ions in the hosts,[5,6] the electrode materials for LIBs are

Dr. H. Zhang, Dr. X. Zhai, Dr. Z. Liu, Dr. X. Tang, Dr. H. Wang, Prof. M. Zhou
Hefei National Laboratory for Physical Sciences at the Microscale, School of Chemistry and Materials Science, University of Science and Technology of China, Hefei 230026, China
E-mail: mzchem@ustc.edu.cn
Dr. X. Cao, Dr. W. He, Prof. Z. Sun
School of Materials Science and Engineering, Southeast University, Nanjing 211189, China
E-mail: zmsun@seu.edu.cn
Dr. Z. Hu, Prof. Z. Wang
National Synchrotron Radiation Laboratory, University of Science and Technology of China, Hefei 230029, China
Prof. Y. Xu
Department of Chemistry, University College London, WC1H 0AJ, London, UK
Dr. W. Zheng
School of Chemistry and Chemical Engineering, Southeast University, Nanjing 211189, China
E-mail: zhengwei22@seu.edu.cn

Hui Zhang, Xingwu Zhai and Xin Cao are co-first authors.

(iD) The ORCID identification number(s) for the author(s) of this article can be found under https://doi.org/10.1002/eem2.12692.

not applicable to SIBs. Many researchers have dedicated much to the electrode material design, particularly in seeking satisfied rate performance during rapid charge/discharge. Corresponding design principle to strike a balance between rate performance and stability remains a challenge recently. Among various electrode materials, Na-free transition metal oxides with intercalation mechanisms stand out due to their excellent structural stability for accommodating ion insertion and extraction.[7,8] Carefully looking into their ion intercalation process, we find that the ability of sodium storage originates from the combination of Na-ion intercalation and capacitance at or near the interface.[9] The larger radius of Na^+ necessitates a more intricate crystalline structure for electrode materials when intercalating, which may induce more time spent and impede charge–discharge performance at high rates. Interface capacitive-like storage happens within a time frame of a few seconds to a few minutes. So the improvement of interface capacitive-like storage is promising to achieve high capacity while also exhibiting excellent rate performance in the same material, without sacrificing stability over long-term sodium storage.

Having a thorough grasp of the characteristics of interface capacitive-like storage is beneficial in formulating precise standards for active materials with intercalation mechanisms. First, the presence of enough electrical conductivity for fast electron movement at or near the interface may enable additional capacitive-like sodium storage, which involves electron transfer or hopping.[9] Unfortunately, most Na-free transition metal oxides, like TiO_2, with intercalation mechanisms are semiconductive with poor electrical conductivity. Second, fast sodium storage that takes place quickly requires a considerable supply of sodium ions. But most Na-free transition metal oxides with intercalation mechanisms lack the necessary ability of surface ion availability, that is, to effectively absorb and retain ions on their surfaces.[10,11] Hence, the synergistic improvement of electrical conductivity and surface ion availability should facilitate fast charge/discharge over a short time.

According to previous literature,[12,13] composites with carbonaceous materials have been widely developed to improve rate capability. But contradictory phase engineering requirements of oxides and carbon raise the difficulties of material design. Taking TiO_2@carbon as a proof of concept example, high treatment temperatures can activate carbon with higher electric conductivity and a clean surface for ion absorption, but will transform anatase TiO_2 into a rutile phase with a lower sodium storage ability. It is significant to design a rational synthetic route to

optimize both phases toward sodium storage at high rates simultaneously. Incorporating N doping in situ is a viable option as it can increase the temperature of the anatase to rutile phase transition of TiO_2 and realize the low-temperature activation of carbon, thus improving the electrical conductivity and ionic uptake of the active materials.

Motivated by this knowledge, we use a molecular design approach with $Ti_3C_2T_z$ MXene (T = −O, −OH, −F, etc.) as the Ti, O sources and scaffold template at the same time. The abundant surface functional terminals of MXenes facilitate strong interactions with molecules with rational-designed functional groups, allowing the formation of a polymer surface coating. To induce an in situ reduction environment during the pyrolysis process, −NH_2 functional groups were chosen here to enable the simultaneous phase engineering of TiO_2 and carbon, as evidenced by in situ pyrolysis monitoring. Nitrogen-doped anatase TiO_2 nanoparticles decorated closely on 2D nitrogen-doped carbon nanosheet (N-TiO_2@NC) can be obtained finally at a high temperature of 800 °C from a topological transformation of MXene templates. Incorporating dual N doping can efficiently enhance the electrical conductivity and Na^+ uptake during fast charge/discharge, thus contributing to excellent rate performance. N-TiO_2@NC nanosheet electrodes were able to maintain a capacity of about 100 mAh g^{-1} at an ultrahigh rate of 5000 mA g^{-1}. Approximately 100 mAh g^{-1} can be obtained

at 2000 mA g^{-1} after 5000 cycles. Such superior rate performance highlights molecular design-enabled phase engineering. This proof of principle demonstration is expected to gain a better comprehension of the interface capacitive-like storage and serve as a direction for creating electrodes with the capability of fast sodium storage.

2. Results and Discussion

2.1. Phase Composition and Morphology Analysis

To realize the molecular design, it is important to choose a suitable molecule with sufficient −NH_2 groups. After a thorough screening, we have identified that 3-aminophenol (3-AF) is an ideal molecule for molecular design given its abundance of −NH_2 groups. $Ti_3C_2T_z$ MXene was chosen as the Ti, O sources and the templates with their detailed morphology and phase characterizations shown in Figure S1, Supporting Information. The entire fabrication process is illustrated in **Figure 1a**, wherein 3-AF can be affixed to the surface functional terminals of MXenes and in situ polymerized with formaldehyde to form a fully covered phenolic resin coating (Figure S2, Supporting Information). After being subjected to a heat treatment at 800 °C, $Ti_3C_2T_z$@3-
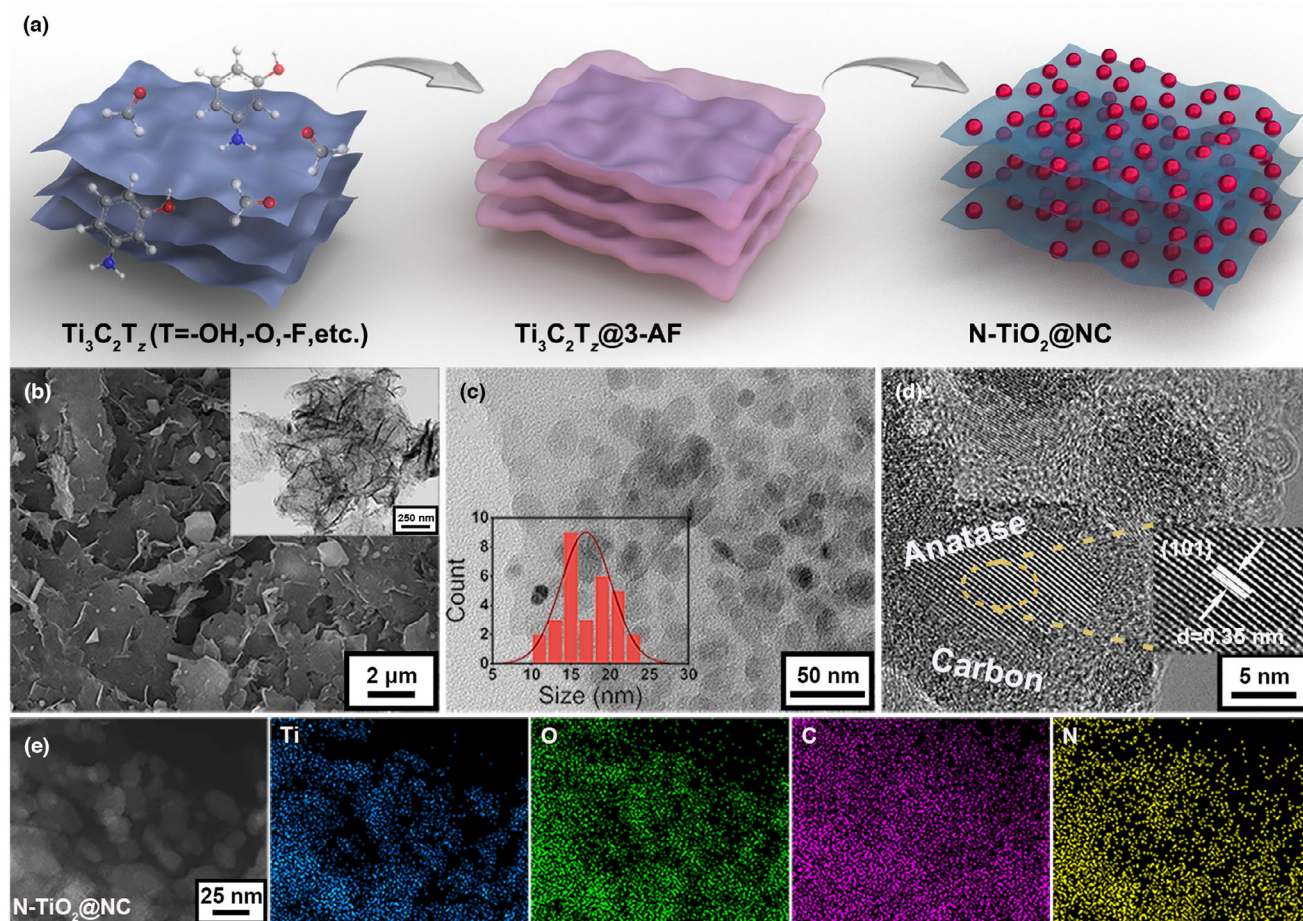

Figure 1. a) Schematic illustration of the synthesis procedure of N-TiO_2@NC nanostructure. b) SEM image of N-TiO_2@NC (inset: TEM image of N-TiO_2@NC); c) TEM image of N-TiO_2@NC under 600 K magnification. d) HRTEM of N-TiO_2@NC and e) the corresponding HAADF STEM-EDX mapping results of Ti, O, C, and N elements recorded from N-TiO_2@NC.

AF was transformed into nanosheets (Figure 1b), similar in morphology to 2D $Ti_3C_2T_z$. The transmission electron microscope (TEM) image in Figure 1c reveals that the nanosheet is composed of many nanoparticles that are tightly attached to an ultrathin nanosheet. These nanoparticles are mostly anatase TiO_2 with a size ranging from 10 to 25 nm (inset in Figure 1c), as evidenced by the (011) lattice fringes (Figure 1d). The amorphous nature of ultrathin nanosheet indicates the existence of amorphous carbon according to the high angle annular dark field scanning transmission electron microscopy (HAADF-STEM) in Figure 1d combined with energy-dispersive X-ray (EDX) mapping in Figure 1e. The TiO_2's ratio is estimated to be 34% in mass, as determined by EDX, thermogravimetric-differential thermal analysis (TG-DTA, Figure S3), and element analyzer. The nanosheet contains evenly distributed N elements, signifying that the N element has been successfully incorporated into both TiO_2 nanoparticles and two-dimensional carbon nanosheets, and thus is denoted as N-TiO_2@NC.

The presence of -NH_2 in phenolic resin is essential for successful phase engineering. For comparison, phenol/formaldehyde (PF) without $-NH_2$ functional groups coated $Ti_3C_2T_z$ (Figure S4, Supporting Information) and pure $Ti_3C_2T_z$ were used as the precursors to assess the origin and effects of N doping. Their pyrolysis products at the same temperature and annealing time are labeled as TiO_2@C and $Ti_3C_2T_z$-HT ($Ti_3C_2T_z$ after heat treatment) as shown in Figures S5 and S6, Supporting Information. The $Ti_3C_2T_z$-HT has an irregular arrangement of particles (Figure S6d,e, Supporting Information). The TiO_2@C exhibits a two-dimensional appearance that is similar to that of N-TiO_2@NC but with larger nanoparticles (Figure S5d,e, Supporting Information). The N contents in the three samples are calculated according to TG-DTA (Figure S3, Supporting Information) and element analyzer (**Figure 2a**) with details in Supporting Information. $Ti_3C_2T_z$-HT and TiO_2@C have a negligible amount of nitrogen, whereas N-TiO_2@NC has a nitrogen content of 3.93 wt%, with 1.26 wt% in the carbon and 2.67 wt% in the TiO_2. We can rule out the possibility that all the N atoms are in TiO_2 and Carbon, as there is no evidence of the existence of TiN or other nitrides in XRD patterns, Raman spectra, HRTEM images, etc. X-ray photoelectron spectroscopy (XPS) spectra mirror this trend in N 1 s spectra with a stronger N signal of N-TiO_2@NC powder (Figure S7a, Supporting Information) compared to those of TiO_2@C (Figure S5a, Supporting Information) and $Ti_3C_2T_z$-HT (Figure S6a, Supporting Information). The N 1s peak is assigned to Ti-N (396.65 eV), pyridine N (398.45 eV), pyrrolic N (401.05 eV), and graphitic N (404.55 eV).[14,15] Additionally, synchrotron radiation X-ray absorption spectroscopy (XAS) of the N spectra (Figure 2b) suggests the existence of π^* pyridinic N, π^* graphitic N, and σ_{C-N}^*, which agrees with the XPS results.[16,17] Compared with TiO_2@C,
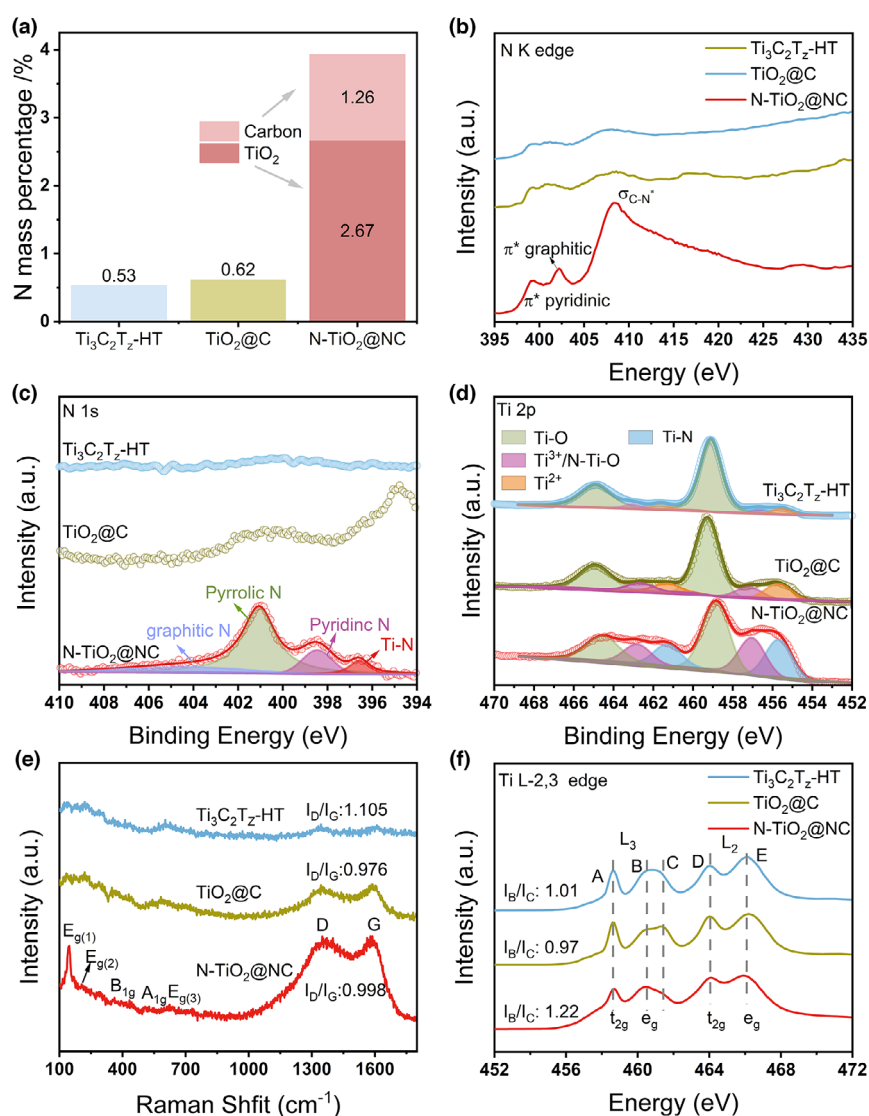

Figure 2. The phase composition and structural analysis of N-TiO_2@NC, TiO_2@C, and $Ti_3C_2T_z$-HT. a) N mass percentage. b) N K-edge of synchrotron radiation XAS spectra. c, d) N 1s and Ti 2p XPS spectra. e) Raman spectra. f) Ti L-edge of synchrotron radiation XAS spectra.

N-TiO_2@NC has a variation of the intensity ratio between D and G (I_D/I_G) in virtue of the successful doping of nitrogen in carbon, which demonstrates the relatively disordered nature of NC.[18,19] As well known, graphitic N, which is located inside the graphene layer, can enhance electric conductivity due to introducing extra free electrons. Meanwhile, pyrrolic N and pyridinic N at the edges or in the defects of the carbon layer can provide active sites for Na^+ adsorption; thus, it is expected to boost the Na^+ storage capacity at high rates.[18]

To TiO_2, the peaks of N belong to Ti-N (455.7 and 460.45 eV) and Ti^{3+}/N-Ti-O (457 and 462.2 eV)[20] in Figure 2d. The shift of Ti-O peaks of N-TiO_2@NC also proves the charge balance caused by the introduction of N for balance. As well known, the anatase–rutile transition has been completed at 800 °C.[17,21] Concerning the phase of TiO_2, both $Ti_3C_2T_z$-HT and TiO_2@C are tetragonal rutile (P42/mnm) phases (Figures S5f and S6f, Supporting Information). But TiO_2 in N-

TiO$_2$@NC contains both the rutile and anatase phases, with the majority being anatase and no TiN impurities according to the Rietveld refined X-ray diffraction (XRD) in Figure S8, Supporting Information. It means that the incorporation of N into TiO$_2$ inhibits the conversion from anatase to rutile. Characteristic Raman active modes and XAS Ti spectra of N-TiO$_2$@NC both evidence the dominant anatase TiO$_2$. As seen in the red line of Figure 2e, five anatase TiO$_2$ peaks with symmetries E$_{g(1)}$, E$_{g(2)}$, B$_{1g}$, A$_{1g}$, and E$_{g3}$ are observed at 147.2, 210.9, 362.2, 507, and 624.2 cm^{-1},[22,23] respectively, which are not found in TiO$_2$@C and Ti$_3$C$_2$T$_z$-HT. The Ti L-edge XAS measurements are used to reveal the complementary valence state and the local structure variation of Ti compounds in Figure 2f. Thanks to the spin–orbit coupling of the Ti 2p states, the Ti L-edge patterns contain two sets of peaks, corresponding to the electron's transition from the 2p$_{3/2}$ and 2p$_{1/2}$ orbitals to the unoccupied 3d orbitals (L$_3$ and L$_2$), which are further split into

t$_{2g}$ and e$_g$ sub-bands.[24,25] The five peaks from left to right are 458.6 (A), 460.5 (B), 461.3 (C), 464.0 (D), and 466.2 eV (E). The intensity ratio of B to C (I$_B$/I$_C$) can be used to distinguish the local symmetry around the Ti atoms and act as a unique identifier for the crystal phases.[26–28] The highest value of I$_B$/I$_C$ (1.22) indicates the dominant anatase phase in N-TiO$_2$@NC.

To trace the origins of N-incorporating more clearly, the affinity between Ti$_3$C$_2$T$_z$ and organic molecules is characterized by Fourier transform infrared spectroscopy (FTIR). In **Figure 3**a, The Ar–NH$_2$ (1630 cm^{-1}),[29] C–N (1280 cm^{-1}),[30] and C–O–C (1100 cm^{-1})[29] can be found in Ti$_3$C$_2$T$_z$@3-AF, while Ti$_3$C$_2$T$_z$@PF hybrids and Ti$_3$C$_2$T$_z$ only exhibit the C=C/benzene ring peak (1640 cm^{-1}).[29] As shown in Figure 3b, the in situ pyrolysis is further tracked by synchrotron vacuum ultraviolet photoionization mass spectrometry (SVUV-PIMS). At a temperature of approximately 400 °C,
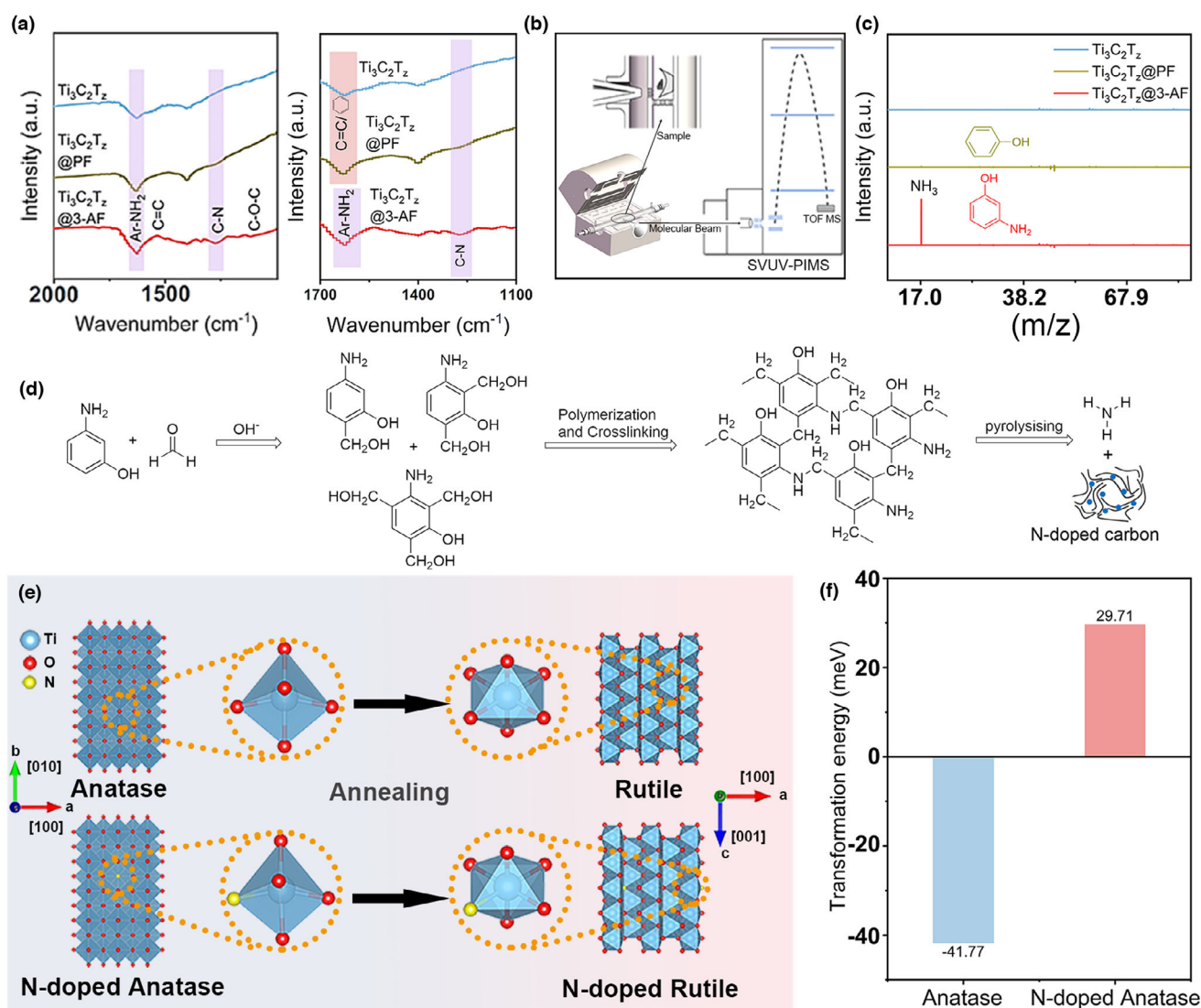

Figure 3. a) FTIR spectra of Ti$_3$C$_2$T$_z$, Ti$_3$C$_2$T$_z$@PF, and Ti$_3$C$_2$T$_z$@3-AF. b) Flow reactor in situ pyrolysis molecular beam sampling-SVUV-PIMS system at the Atomic & Molecular Physics Beamline (BL09U) of NSRL. c) Synchrotron vacuum ultraviolet photoionization mass spectra of Ti$_3$C$_2$T$_z$, Ti$_3$C$_2$T$_z$@PF, and Ti$_3$C$_2$T$_z$@3-AF. d) Scheme of synthesis and pyrolysis process of 3-AF. e) Scheme of phase transition between anatase/N dope anatase and rutile/N dope rutile. Blue, red, and yellow spheres represent Ti, O, and N atoms, respectively. f) Calculation of transformation energy from the anatase TiO$_2$ to rutile TiO$_2$.

NH_3 was observed obviously, providing a reduction atmosphere and supplying a nitrogen source to form NC and N-doped TiO_2, as demonstrated in Figure 3c. Overall, the entire process of NC formation is summarized in Figure 3d. The polymerization and crosslinking results in the amorphous carbon nanosheets with $Ti_3C_2T_z$ as the templates. The molecular design of introducing $-NH_2$ functional groups plays a key role in the online generation of NH_3 during pyrolysis to realize N doping. Of significance, the N introduction raises the difficulties of the anatase to rutile transformation, which is dependent directly on the transformation energy (Δ_{TE}) from the anatase TiO_2 to rutile TiO_2. As seen in Figure 3e,f, the transformation of anatase TiO_2 to rutile TiO_2 is thermodynamically preferred, as evidenced by its negative formation energy of -41.77 meV. However, when N doping is applied, the formation energy changes to a positive value of 29.71 meV, suggesting that additional energy is needed to overcome the high barriers. As such, anatase $N–TiO_2$ can be obtained at higher temperatures of 800°C, which would further benefit to activated carbon to increase the electric conductivity and surface ion availability.[18] The results illustrate the importance of molecular design in controlling the phases of TiO_2 and carbon with superior sodium storage simultaneously, which can lead to the improved electrochemical performance of N-TiO_2@NC.

2.2. Electrochemical Performance

The electrochemical performances of N-TiO_2-@NC (N-doped TiO_2@N-doped carbon), TiO_2@C (TiO_2@carbon), and $Ti_3C_2T_z$-HT ($Ti_3C_2T_z$ after heating) were evaluated by Cyclic Voltammetry (CV). Figure 4a exhibits the typical CV curves of the three samples at 0.1 mV s^{-1} in 0.01–3 V (the 3rd cycle) without any influence of SEI formation. The comparable CV shapes without obvious redox peaks prove the similar sodium-ion storage mechanism of interface capacitive-like storage. Higher current responses indicate a strong sodium storage ability of N-TiO_2@NC. The characteristic curves of charge/discharge at 50 mA g^{-1} in Figure S9, Supporting Information, mirror the trends of CV curves. The absence of plateaus and the relatively straight charge/discharge lines indicate a capacitive performance. Figure 4b lists their cycling performance at 50 mA g^{-1}. The N-TiO_2@NC shows the best behavior with a capacity of ~216 mA h g^{-1} after 500 cycles with an 86.1% capacity retention of its initial capacity at the third cycle. In contrast, only ~83 and 64 mA h g^{-1} are delivered by the $Ti_3C_2T_z$-HT and TiO_2@C electrodes, respectively. More exciting performance is the rate capacities in Figure 4c with the discharge/charge profiles in Figure S10, Supporting Information. The N-TiO_2@NC electrode has a significantly higher specific capac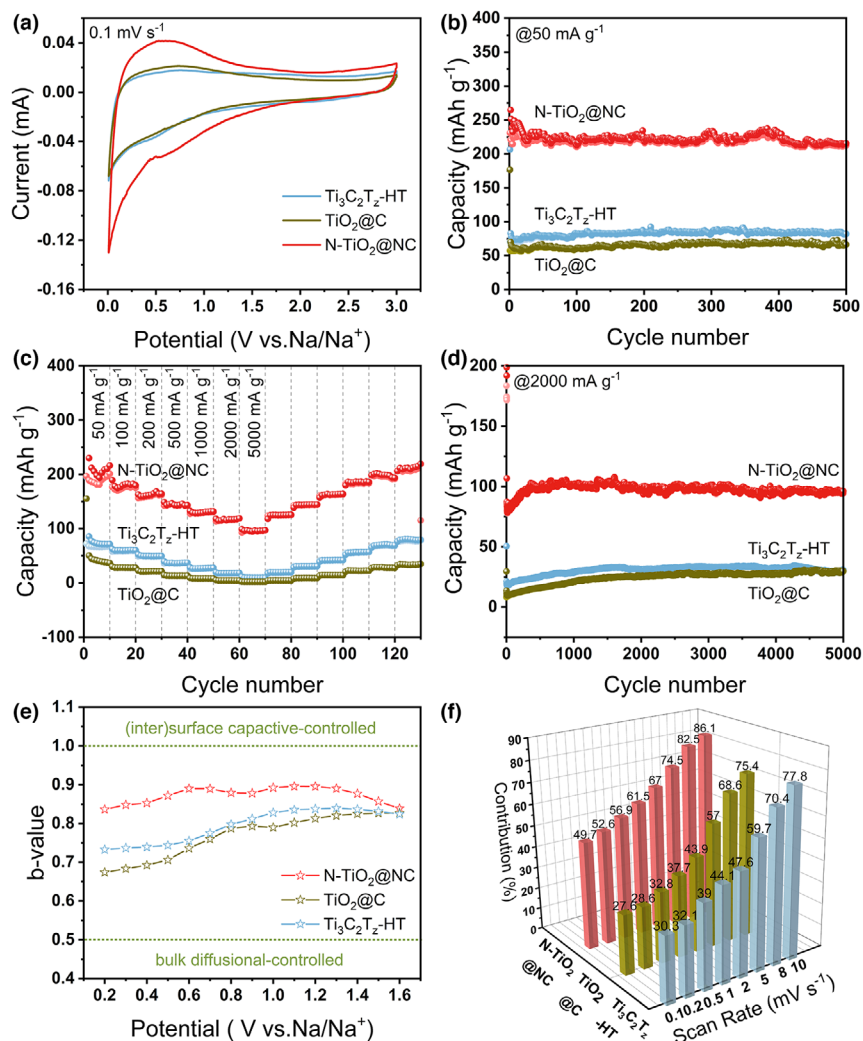ity than the $Ti_3C_2T_z$-HT and TiO_2@C electrodes when tested at current densities of 50, 100, 200, 500, 1000, 2000, and 5000 mA g^{-1}, with values of 216, 182, 164, 143, 131, 118, and 97 mAh g^{-1}, respectively, compared to 77, 60, 49, 36, 27, 18.4, and 9.4 mAh g^{-1} for $Ti_3C_2T_z$-HT and 50.5, 28.1, 21.1, 13.1, 8.2, 4.4, 2.1 mAh g^{-1} for TiO_2@C. When the current densities return, all three electrodes exhibit reversible capacities. Figure 4d further reveals the long-term cycling stability. The N-TiO_2@NC electrode has a capacity of ~100 mAh g^{-1} after 5000 cycles at 2000 mA g^{-1}, which is three times and four times greater than that of the $Ti_3C_2T_z$-HT and TiO_2@C electrodes, respectively.

As mentioned before, the total capacity of the N-TiO_2@NC electrode can be divided into two parts: (i) capacitive process related to the (inter)surface charge transfer and (ii) diffusion-limited redox process related to the bulky reactions. To explore the contribution of these two

Figure 4. a) The third CV curves of N-TiO_2@NC, TiO_2@C, and $Ti_3C_2T_z$-HT measured at 0.1 mV s^{-1}. b) Cycling performance of N-TiO_2@NC, TiO_2@C, and $Ti_3C_2T_z$-HT at 50 mA g^{-1}. c) The rate capability of N-TiO_2@NC, TiO_2@C, and $Ti_3C_2T_z$-HT at various current densities. d) Cycling performance of N-TiO_2@NC, TiO_2@C, and $Ti_3C_2T_z$-HT at 2000 mA g^{-1} for 5000 cycles. e) b-values of N-TiO_2@NC, TiO_2@C, and $Ti_3C_2T_z$-HT calculated from 0.2 to 1.6 V. f) The column diagram of the capacitive contribution ratio of N-TiO_2@NC, TiO_2@C, and $Ti_3C_2T_z$-HT at various scan rates.

different behaviors, b-values are used and fitted with the formula of $i = av^b$ (i is current and v is scan rate)[31] according to the CV curves at different scan rates in Figure S11, Supporting Information. The b-values of N-TiO$_2$@NC are closer to 1 than those of TiO$_2$@C and Ti$_3$C$_2$T$_z$-HT in the potential range from 0.2 to 1.6 V in Figure 4e, indicating that the capacities of N-TiO$_2$@C are more capacitive-controlled. The interface capacitance-like contribution at a given scan rate (v) can be further quantitatively differentiated by the formula as follows, $i = k_1v + k_2v^{1/2}$.[32] By solving for the adjustable values (k_1, k_2) at each potential, it becomes possible to distinguish between diffusion-controlled currents, which are proportional to v, and capacitive-like currents, which are proportional to $v^{1/2}$. As displayed in Figure 4f and Figures S12–S14, Supporting Information, the capacitive contributions of the three electrodes increase as the scan rate raising from 0.1 to 10 mV s^{-1}. At a low scan rate of 0.2 mV s^{-1}, more than 50% of the total capacity is attributable to capacitance. This ratio increases to 86.1% when the scan rate increases to 10 mV s^{-1}, that is, the whole capacity mainly originates from the interface capacitance. The N-TiO$_2$@NC electrode exhibits faster sodium storage kinetics than TiO$_2$@C and Ti$_3$C$_2$T$_z$-HT electrodes, resulting in higher capacitive contributions at the same scan rates and thus better performance at high rates.

2.3. In-depth discussion of electrochemical behaves

To better grasp the enhanced rate performance, the charge storage mechanism of the N-TiO$_2$@NC electrode is observed first. Shown in **Figure 5**a, the characteristic TiO$_2$ E$_{g(1)}$ peaks at ~149 cm^{-1} have

reversible shifts during the first charge/discharge cycles in a half-cell versus Na/Na$^+$ at 50 mA g^{-1}, indicating the ion intercalated process instead of conversion and alloy reactions. The baseline kept jumping at the end of charging, likely ascribed to a long time exposure of the electrode under the laser. The ex situ Raman spectra (Figure 5b) show that the TiO$_2$ E$_{g(1)}$ peaks undergo revisable shifts after charging/discharging at different voltages during the first and second cycles. During discharge, the E$_{g(1)}$ peak undergoes a slight red shift from 148.9 to 151.5 cm^{-1} and then returns closely to its original position upon full charge. Thus, it is reasonable to assume the revisable intercalation/deintercalation of Na$^+$. The Ti L-edge of synchrotron radiation XAS spectra after charge/discharge at different cutoff voltages (Figure 5c) displays the charge compensation of Ti during Na$^+$ insertion and extraction. Ti's intensities of L$_2$ and L$_3$ peaks demonstrate a reversible correlation with Na$^+$ electrochemistry, becoming more prominent with the entrance of Na$^+$ and diminishing with its release, indicating the electronic connection between Ti and Na$^+$.[33] In addition, the N-TiO$_2$@NC electrode displays high reversibility, as the peak intensity remains unchanged when the same voltage is applied. This valence change is further illustrated in the high-resolution XPS of Ti spectra in Figure 5d, where the peaks of Ti^{3+} become dominant upon discharging after long cycling at a high current density of 3000 mA g^{-1}. It reveals a Na$^+$ interface-redox capacitive behavior in the N-TiO$_2$@NC without any Ti^0 from the conversion mechanism.

The electrochemical impedance spectroscopy (EIS) spectra of N-TiO$_2$@NC, TiO$_2$@C, and Ti$_3$C$_2$T$_z$-HT when discharged to 0.01 V after 5 and 50 cycles are displayed in Figure 5e at 2000 mA g^{-1} and Figure S15, Supporting Information, at 50 mA g^{-1}. The lowest
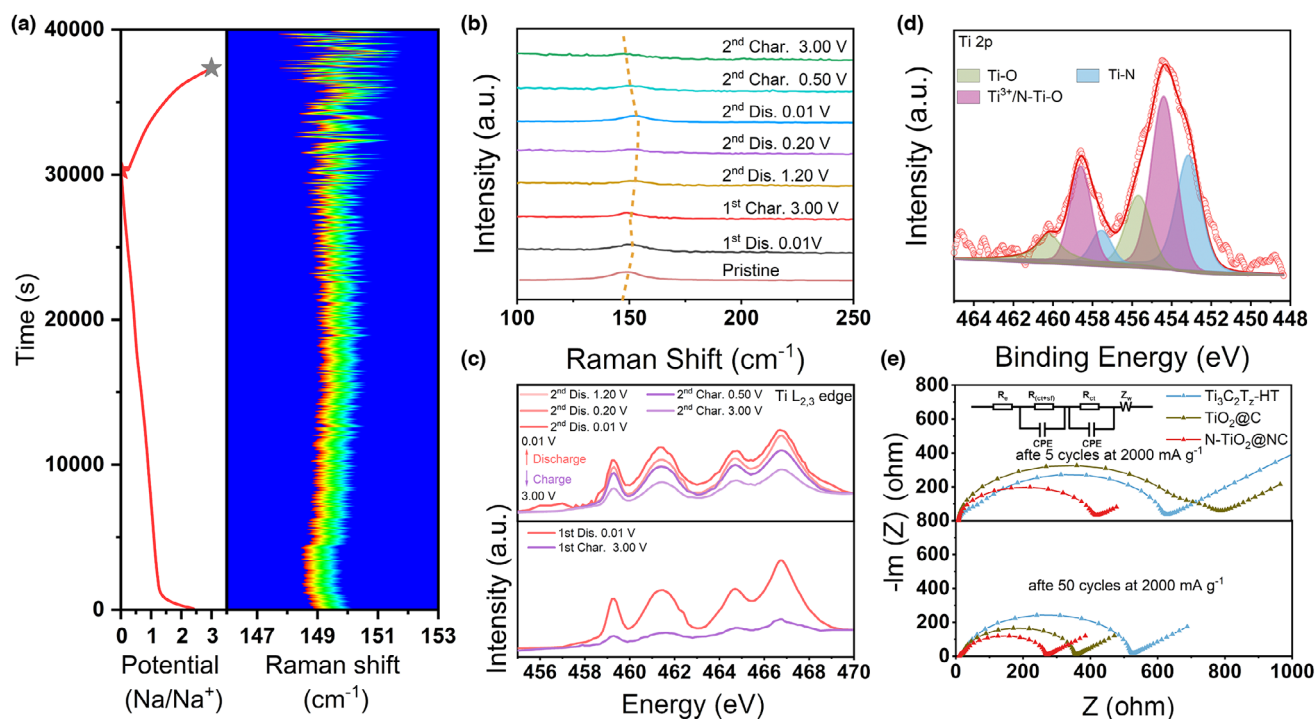

Figure 5. a) In situ Raman spectra of N-TiO$_2$@NC, as well as the corresponding first charge/discharge cycles in a half cell versus Na at 50 mA g^{-1}. b) Ex situ Raman spectra of pristine N-TiO$_2$@NC and after charging/discharging at different voltages of first and second at 50 mA g^{-1}. c) Ti L$_{2,3}$-edge of synchrotron radiation XAS spectra of N-TiO$_2$@NC after charging/discharging at different voltages of first and second under at 50 mA g^{-1}. d) Ti 2p XPS spectra of N-TiO$_2$@NC after long cycles at 3000 mA g^{-1}. e) EIS spectra of N-TiO$_2$@NC (discharged to 0.01 V) after 5 cycles and 50 cycles at 2000 mA g^{-1}, respectively.

interface charge transfer resistance (R_{ct}) for N-TiO$_2$@NC is observed, enabling the fast Na$^+$ transfer. After 50 cycles, the reduced R_{ct} values for N-TiO$_2$@NC at different current densities are probably related to the continuous activation of active materials and opening of the structure of electrodes, which allows electrolyte penetration. As a result, the rate performance is largely improved.

To gain a comprehensive understanding of phase engineering toward electrochemical performance, density functional theory (DFT) calculations were executed to explore the function of dual N doping.

According to the HRTEM images, we first set up models of (100) facets of TiO (vertical to the {011}a facets) in N-TiO$_2$@NC, TiO$_2$@C, and Ti$_3$C$_2$T$_z$-HT for illumination (**Figure 6a–c**). As mentioned before, electrical conductivity and surface ion availability are two key factors for fast charge/discharge. On one side, the density of states (DOS) was performed to assess electrical conductivity (Figure 6d). Without any carbon, Ti$_3$C$_2$T$_z$-HT is a semiconductor (pure rutile TiO$_2$) with no electronic states crossing the Fermi level, resulting in relatively poor electronic conductivity. In contrast, N-TiO$_2$@NC and TiO$_2$@C are
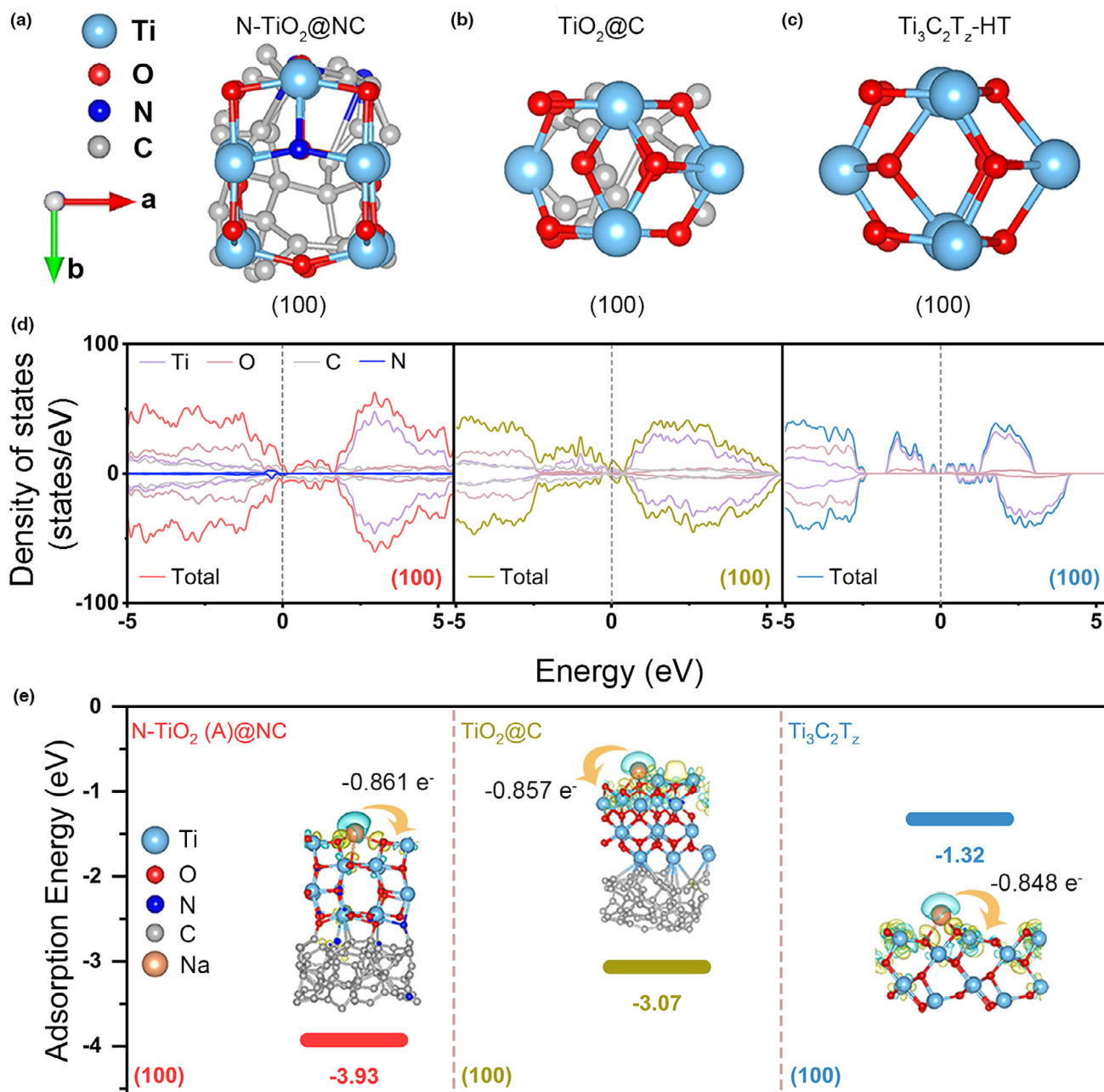

Figure 6. a–c) (100) Facet models of N-TiO$_2$@NC, TiO$_2$@C, and Ti$_3$C$_2$T$_z$-HT. d) Total/local densities of states (TDOS/PDOS) of N-TiO$_2$@NC, TiO$_2$@C, and Ti$_3$C$_2$T$_z$-HT. e) Na$^+$ absorption energy of N-TiO$_2$ @NC, TiO$_2$ @C, and Ti$_3$C$_2$T$_z$-HT for (100) plane. Insets show the corresponding charge-density differences and Bader charge analysis. Yellow region indicates charge accumulation while cyan means charge depletion.

metallic in nature and possess enhanced electronic conductivity. Note that the existence of N contributes more electronic density around the Fermi level, indicating the best electronic conductivity of N-TiO$_2$@NC. On the other side, surface ion availability can be evaluated by Na$^+$ absorption ability. So we optimized the structures after Na$^+$ absorption as shown in Figure 6e. Na$^+$ has the highest affinity for the (100) facets of N-TiO$_2$@NC, with an adsorption energy of -3.93 eV, followed by TiO$_2$@C (-3.07 eV) and Ti$_3$C$_2$T$_z$-HT (-1.32 eV). Furthermore, the Bader charge analysis and charge density differences are used to understand Na$^+$ adsorption and the associated charge transfers.[34] The amount of charge donated by the Na$^+$ ions to the (100) facets for N-TiO$_2$@NC, TiO$_2$@C, and Ti$_3$C$_2$T$_z$-HT is 0.861, 0.857, and 0.848 e, respectively, by the strength of Na$^+$ adsorption energy and charge density differences, that is, the Na$^+$ adsorption ability becomes more powerful with the increased extent of charge transfer. Similar trends of electrical conductivity and surface ion availability can also be found in (001) facets of N-TiO$_2$@NC, TiO$_2$@C, and Ti$_3$C$_2$T$_z$-HT shown in Figures S16–S19, Supporting Information. All the results highlight the dual-phase engineering toward the optimized electronic transport and surface ion adsorption, thus contributing to better sodium storage at high rates.

3. Conclusion

Overall, we used a molecular design strategy to realize phase engineering of dual-phased MXene derivatives (TiO$_2$ and carbon). Functional terminals of MXene can interact strongly with molecules that have been designed with specific functional groups and then solidified through in situ crosslinking. For example, the selection of $-$NH$_2$ functional groups was made to facilitate the concurrent manipulation of the phases of TiO$_2$ and carbon, as demonstrated by in situ pyrolysis monitoring. The incorporation of N into TiO$_2$ and carbon has successfully addressed the challenge of achieving a balancing act between the activity of anatase TiO$_2$, which can maintain stability only at low temperatures, and carbon activation at high temperatures for higher sodium storage ability. The higher energy barrier of the anatase-to-rutile transformation and improved transformation temperature facilitated this achievement. As a result, the electrodes exhibit enhanced electrical conductivity and surface Na$^+$ availability, contributing to higher interface capacitive-like storage and superior rate performance. The N-TiO$_2$@NC nanosheet electrodes have maintained a capacity of over 100 mAh g^{-1} at an ultra-high rate of 5000 mA g^{-1} and approximately 100 mAh g^{-1} can be obtained at 2000 mA g^{-1} after 5000 cycles. By utilizing this molecular design-enabled phase engineering, it may be possible to extend to other MXenes such as Nb$_2$CT$_z$, Mo$_2$CT$_z$, and V$_2$CT$_z$. This approach holds the potential to inspire further development and guide future research toward designing high-rate energy storage materials based on MXenes.

4. Experimental Section

Materials: The materials used were Ti$_3$AlC$_2$ (Foshan XinXi Technology Co., Ltd.), ultrapurified water (Smart-S30 ultrapure water system from Hitech Instruments CO., Ltd), HCl (Sinopharm Chemical Reagent), lithium fluoride (Aladdin Reagent), formaldehyde solution (37%wt, Macklin), 3-Aminophenol (Aladdin Reagent),

phenol (Aladdin Reagent), and ammonium hydroxide (Sinopharm Chemical Reagent).

Materials preparation: *Synthesis of Ti$_3$C$_2$T$_z$*—To obtain Ti$_3$C$_2$T$_z$, typically, 5 g of LiF was mixed with 100 mL of 9 M HCl and stirred continuously at 300 rpm for 30 min to make the etching solution. Then, 5 g of Ti$_3$AlC$_2$ powder was slowly added to the above solution and the reaction mixture was stirred at 300 rpm for 24 h at room temperature. After that, the acidic mixture was washed with ultra-purified water (Smart-S30 ultrapure water system from Hitech Instruments CO., Ltd) by centrifugation (3 min per cycle, 3500 rpm) until pH 6–7 was reached. Then, the solution bubbled with N$_2$, was sonicated at 200 W for 1 h, and centrifuged at 1328 g for 1 h to obtain the suspension of Ti$_3$C$_2$T$_z$.

Synthesis of Ti$_3$C$_2$T$_z$@3-AF—To synthesize Ti$_3$C$_2$T$_z$@3-AF, typically, 100 mL of 5 mg mL^{-1} suspension of Ti$_3$C$_2$T$_z$ was poured into 50 mL of 10 mg mL^{-1} anhydrous alcohol solution of 3-aminophenol and stirred for 30 min at 50 °C in a water bath at 500 rpm. Subsequently, 250 µL of ammonium hydroxide and 500 µL of formaldehyde solution were successively added to the solution and stirred at 500 rpm for 2 h at 50 °C. After centrifugation, freeze-drying, and vacuum drying at 60 °C, the complex of 3-aminophenol/formaldehyde (3-AF) and Ti$_3$C$_2$T$_z$, denoted as Ti$_3$C$_2$T$_z$@3-AF can be obtained.

Synthesis of Ti$_3$C$_2$T$_z$@PF—To synthesize Ti$_3$C$_2$T$_z$@PF, typically, 20 mL of 5 mg mL^{-1} suspension of Ti$_3$C$_2$T$_z$ was poured into 10 mL of 10 mg mL^{-1} anhydrous alcohol solution of phenol, and stirred for 30 min at 50 °C in a water bath at 500 rpm. Subsequently, 50 µL of ammonium hydroxide and 100 µL of formaldehyde solution were successively added to the solution and stirred at 500 rpm for 2 h at 50 °C. After centrifugation, freeze-drying, and vacuum drying at 60 °C, the complex of phenol/formaldehyde (PF) and Ti$_3$C$_2$T$_z$, denoted as Ti$_3$C$_2$T$_z$@PF, can be obtained.

Synthesis of N-TiO$_2$@NC, Ti$_3$C$_2$T$_z$-HT, and TiO$_2$@C—To synthesize N-TiO$_2$@NC, 120 mg of Ti$_3$C$_2$T$_z$@3-AF was heated to 800 °C at a rate of 5 °C/min. After soaking at 800 °C for 6 h, the furnace was cooled down. The whole process was carried out in an Ar-flowing atmosphere. For comparison, Ti$_3$C$_2$T$_z$ and Ti$_3$C$_2$T$_z$@PF were heat treated under the same conditions, and the final products were noted as Ti$_3$C$_2$T$_z$-HT and TiO$_2$@C, respectively.

Material characterizations: Material characterizations were conducted by SEM (Quanta FEG 250), TEM (H-7650), HRTEM (JEM-2100F), the high-angle annular dark field (HAADF) scanning transmission electron microscopy (STEM) (JEM-F200 multi-purpose electron microscope). X-ray photoelectron spectrometer (ESCALAB 250Xi), XRD patterns (SmartLabTM 9 kW with Cu radiation ($\lambda = 1.54$ Å).), Raman (LabRAM HR 532 nm laser spectrometer (HORIBA Scientific)), and in situ Raman (WITec Alpha 300R). The XAFS data were collected from Beamlines MCD-A and MCD-B (Soochow Beamline for Energy Material) at the National Synchrotron Radiation Laboratory (NSRL).

The in situ pyrolysis was carried out at the Atomic & Molecular Physics Beamline (BL09U) of NSRL. A flow reactor is connected to the synchrotron vacuum ultraviolet radiation-photoionization mass spectrometry (SVUV-PIMS) through a tapered quartz nozzle. The mass resolution of SVUV-PIMS is ca. 5000 at m/z 100 and the detection limit is ca. 0.1 ppm. The precursor Ti$_3$C$_2$T$_z$@3-AF (or Ti$_3$C$_2$T$_z$@PF, or Ti$_3$C$_2$T$_z$)) was put inside a slender quartz boat, which was put in the middle of the flow reactor. The dilution gas of Ar was controlled by mass flow controllers (MKS) and the pressure of the reactor was maintained at 760 torr. The temperature of the reactor was increased from 50 to 1000 K with a heating rate of 20 K/min. The photon energy was 11.5 eV. Before loading the samples, the quartz boats were heated in a muffle furnace under 1000 °C for 10 min, this procedure effectively reduced impurity content and enabled the decomposition process without interference.

Computational methods: The spin-polarized density functional theory (DFT) calculations were performed by using the Vienna Ab initio Simulation Package (VASP).[35,36] A plane wave energy cutoff was set to 500 eV. The N-TiO$_2$@NC, TiO$_2$@C, and Ti$_3$C$_2$T$_z$-HT (001/100) plane was modeled for geometry optimizations. The Van der Waals (vdW) interactions were considered using the DFT-D3 method.[37] A vacuum distance of 15 Å was imposed to avoid interactions between periodic slabs. The DFT + U method was adopted to evaluate the on-site Coulomb interactions and exchange interactions in the localized d-orbital. Here, we applied a 4.2 eV U-J value for Ti d-electrons in this work.[38] The atomic positions and lattice constants were fully optimized until the total energy and residual forces on each atom dropped below 10^{-5} eV and 0.05 eV/Å,

respectively. The adsorption energy (E_{ads}) of Na^+ was determined by the following equation:

$$E_{ads} = E_{total} - E_{slab} - E_{Na}$$

where E_{slab} and E_{total} are total energies before and after the Na^+ adsorption, respectively. E_{Na} is the energy of the Na atom in its bulk phase.

Electrochemical measurement: SIB tests were carried out using CR2032 coin cells with sodium foils as the counter and reference electrodes. Galvanostatic charge and discharge (GCD) profiles were investigated with a NETWARE battery tester (MHW-200, Shenzhen, China). Cyclic voltammetry (CV) studies were tested on a VSP-3E electrochemical workstation (Biologic, France) at a series of scan rates from 0.1 to 20 mV s^{-1}. Electrochemical impedance spectroscopy (EIS) measurements were performed in coin cells with Na metal as counter/reference electrodes. The EIS tests were conducted on the same electrochemical workstation in the frequency range of 1–10 MHz with an AC amplitude of 5 mV. The working electrodes (16 mm in diameter) consist of active material (N-TiO$_2$@NC, Ti$_3$C$_2$T$_z$-HT, and TiO$_2$@C), super P, CNT (5 wt%), and carboxymethyl cellulose (CMC) with a weight ratio of 7:1:1:1 in deionized water. The obtained slurries were coated on Cu foils and dried at 80 °C for 12 h in a vacuum oven. The average mass loading on the electrodes was 0.3 ± 0.1 mg cm^{-2}. The separator was a glass fiber filter (GF\B, Whatman, UK), and the electrolyte was 1 M NaClO$_4$ in polycarbonate (PC) with 5% FEC. These cells were assembled inside an Ar-filled glove box (MIKROUNA, China) (H$_2$O < 0.01 ppm, O$_2$ < 0.01 ppm).

Conflict of Interest

The authors declare no conflict of interest.

Supporting Information

Supporting Information is available from the Wiley Online Library or from the author.

[1] M. S. Islam, C. A. J. Fisher, *Chem. Soc. Rev.* **2014**, 43, 185.

[2] P. K. Nayak, L. T. Yang, W. Brehm, P. Adelhelm, *Angew. Chem. Int. Ed.* **2018**, 57, 102.

[3] C. Feng, X. Huang, *Acc. Chem. Res.* **2018**, 51, 2314.

[4] M. G. Alexey, *Energy Mater.* **2023**, 3, 300010.

[5] H. Liang, L. Liu, N. Wang, W. Zhang, C.-T. Hung, X. Zhang, Z. Zhang, L. Duan, D. Chao, F. Wang, Y. Xia, W. Li, D. Zhao, *Adv. Mater.* **2022**, 34, 2202873.

[6] Z. Wang, W. Jin, X. Huang, G. Lu, Y. Li, *Chem. Rec.* **2020**, 20, 1198.

[7] M. Zhou, Y. Xu, Y. Lei, *Nano Today* **2018**, 20, 33.

[8] H. Wang, Q. Yang, N. Zheng, X. Zhai, T. Xu, Z. Sun, L. Wu, M. Zhou, *Nano Res.* **2023**, 16, 4107.

[9] Q. Li, H. Wang, X. Tang, M. Zhou, H. Zhao, Y. Xu, W. Xiao, Y. Lei, *Adv. Funct. Mater.* **2021**, 31, 2101081.

[10] Y. Mi, L. Wen, Z. Wang, D. Cao, R. Xu, Y. Fang, Y. Zhou, Y. Lei, *Nano Energy* **2016**, 30, 109.

[11] L. Wen, M. Zhou, C. Wang, Y. Mi, Y. Lei, *Adv. Energy Mater.* **2016**, 6, 1600468.

[12] L. Dai, D. W. Chang, J.-B. Baek, W. Lu, *Small* **2012**, 8, 1130.

[13] Y. Zhao, L. P. Wang, M. T. Sougrati, Z. Feng, Y. Leconte, A. Fisher, M. Srinivasan, Z. Xu, *Adv. Energy Mater.* **2017**, 7, 1601424.

[14] T. Susi, T. Pichler, P. Ayala, *Beilstein J. Nanotechnol.* **2015**, 6, 177.

[15] Y. M. Shul'ga, V. N. Troitskii, *Powder Metall. Met. Ceram.* **1979**, 18, 681.

[16] Z. Zhang, L. Yu, Y. Tu, R. Chen, L. Wu, J. Zhu, D. Deng, *Cell Rep. Phys. Sci.* **2020**, 1, 100145.

[17] F. De Angelis, C. Di Valentin, S. Fantacci, A. Vittadini, A. Selloni, *Chem. Rev.* **2014**, 114, 9708.

[18] J. Zhu, C. Chen, Y. Lu, Y. Ge, H. Jiang, K. Fu, X. Zhang, *Carbon* **2015**, 94, 189.

[19] S. Liu, H. Yang, X. Huang, L. Liu, W. Cai, J. Gao, X. Li, T. Zhang, Y. Huang, B. Liu, *Angew. Chem. Int. Ed.* **2018**, 28, 1800499.

[20] P. Yang, D. Chao, C. Zhu, X. Xia, Y. Zhang, X. Wang, P. Sun, B. K. Tay, Z. X. Shen, W. Mai, H. J. Fan, *Adv. Sci.* **2016**, 3, 1500299.

[21] D. A. H. Hanaor, C. C. Sorrell, *J. Mater. Sci.* **2011**, 46, 855.

[22] F. Tian, Y. Zhang, J. Zhang, C. Pan, *J. Phys. Chem. C* **2012**, 116, 7515.

[23] O. Frank, M. Zukalova, B. Laskova, J. Kürti, J. Koltai, L. Kavan, *Phys. Chem. Chem. Phys.* **2012**, 14, 14567.

[24] L. Pan, M. Ai, C. Huang, L. Yin, X. Liu, R. Zhang, S. Wang, Z. Jiang, X. Zhang, J.-J. Zou, W. Mi, *Nat. Commun.* **2020**, 11, 418.

[25] Y. Harada, M. Watanabe, R. Eguchi, Y. Ishiwata, M. Matsubara, A. Kotani, A. Yagishita, S. Shin, *J. Electron Spectrosc.* **2001**, 114-116, 969.

[26] J. Li, L. Liu, T.-K. Sham, *Chem. Mater.* **2015**, 27, 3021.

[27] D. Maganas, S. DeBeer, F. Neese, *Inorg. Chem.* **2014**, 53, 6374.

[28] W. Wang, M. Wu, P. Han, Y. Liu, L. He, Q. Huang, J. Wang, W. Yan, L. Fu, Y. Wu, *ACS Appl. Mater. Interfaces* **2019**, 11, 3061.

[29] D.-S. Bin, Z.-X. Chi, Y. Li, K. Zhang, X. Yang, Y.-G. Sun, J.-Y. Piao, A.-M. Cao, L.-J. Wan, *J. Am. Chem. Soc.* **2017**, 139, 13492.

[30] J. Zhao, R. Luque, W. Qi, J. Lai, W. Gao, M. R. H. S. Gilani, G. Xu, *J. Mater. Chem. A* **2015**, 3, 519.

[31] H. Lindström, S. Södergren, A. Solbrand, H. Rensmo, J. Hjelm, A. Hagfeldt, S.-E. Lindquist, *J. Phys. Chem. B* **1997**, 101, 7717.

[32] M. Sathiya, A. S. Prakash, K. Ramesha, J. M. Tarascon, A. K. Shukla, *J. Am. Chem. Soc.* **2011**, 133, 16291.

[33] K. Zhu, S. Wei, H. Shou, F. Shen, S. Chen, P. Zhang, C. Wang, Y. Cao, X. Guo, M. Luo, H. Zhang, B. Ye, X. Wu, L. He, L. Song, *Nat. Commun.* **2021**, 12, 6878.

[34] G. Henkelman, A. Arnaldsson, H. Jónsson, *Comput. Mater. Sci.* **2006**, 36, 354.

[35] G. Kresse, J. Furthmüller, *Physical Review B* **1996**, 54, 11169.

[36] G. Kresse, D. Joubert, *Phys. Rev. B* **1999**, 59, 1758.

[37] S. Grimme, J. Antony, S. Ehrlich, H. Krieg, *J. Chem. Phys.* **2010**, 132, 154104.

[38] W. Tang, J. Xuan, H. Wang, S. Zhao, H. Liu, *J. Power Sources* **2018**, 384, 249.